



Universal construction of sulfur doped molybdenum-based nanosheets for enhanced hydrogen evolution in a wide pH range

Minghao Hu ^a, Baocang Liu ^{a,*}, Hengyi Chen ^a, Xuan Xu ^a, Peng Jing ^a, Xiaolei Guo ^a, Rui Yang ^a, Xiaoyang Wang ^a, Rui Gao ^{a,*}, Jun Zhang ^{a,b,**}

^a School of Chemistry and Chemical Engineering & Inner Mongolia Engineering and Technology Research Center for Catalytic Conversion and Utilization of Carbon Resource Molecules, Inner Mongolia University, 49 Xilingoule South Road, Hohhot 010020, PR China

^b Inner Mongolia Academy of Science and Technology, 70 Zhaowuda Road, Hohhot 010010, PR China



ARTICLE INFO

Keywords:

Molybdenum-based compounds
S-doping
Synergistic effect
PH-universal
Hydrogen evolution reaction

ABSTRACT

Rational designing and fabricating catalysts with abundant exposed active sites and optimized electronic structure is of essential to boost electrocatalytic performance. In this study, well-organized porous nanosheets of sulfur-doped molybdenum-based compounds on carbon cloth (S-MoX_n/CC, S-MoX_n = S-MoP, S-Mo₂C, S-MoN, and S-MoO₃) are universally constructed via in situ topological transformation from the MoS₂ nanosheets as self-supported electrodes for pH-universal hydrogen evolution reaction (HER). Various structural characterizations show that the S-MoX_n nanosheets with abundant nanopores and edges endowing them with plentiful exposed active sites, high mass transfer efficiency, and good conductivity. As a result, these S-MoX_n/CC electrodes, especially S-MoP/CC exhibits superior HER performance with low overpotentials of 75, 75, and 127 mV at 10 mA cm⁻¹ in acidic, alkaline, and neutral electrolytes, superior to the MoX_n/CC counterparts. Theoretical calculations reveal that the synergy between S dopant and MoX_n can effectively alter the electronic structure of S-MoX_n, thus enhancing the HER performance.

1. Introduction

Hydrogen, a green and renewable source, is a promising alternative to fossil fuels due to its high gravimetric-energy-density and zero-carbon emission [1]. Electrocatalytic hydrogen evolution reaction (HER) by water splitting is a viable and sustainable route to generate high-purity hydrogen [2]. By far, Pt/C is still the most effective electrocatalyst for HER, but the large-scale application is severely impeded by its high price and low abundance [3]. Hence, developing inexpensive, stable, and highly active electrocatalysts in pH-universal for HER is of great importance for the achievement of hydrogen economy.

Amidst the current noble-metal-free catalysts, molybdenum-based compounds, such as MoS₂, MoC_x, MoP, MoN_x, and MoO_x, have demonstrated promising catalytic activity and stability for HER due to their natural abundance and Pt-like *d*-band electronic configuration [4–10]. Although these reported molybdenum-based compounds display appreciable HER performance, it is still needed to further

promote their HER activity and stability to satisfy the actual requirement. To date, various strategies, including phase engineering [4], doping engineering [5,6], nanocarbon hybridization [7,10,11], surface/interface engineering [8,12,13], and defect engineering [14], have been developed to increase the number of exposed active sites or/and enhance the intrinsic activity of active sites. However, these molybdenum-based catalysts still show unsatisfactory HER activities possibly due to their undesirable nanostructures, which are inconducive to the exposure of active sites and charge/mass transfer [12,13]. In addition, the high formation temperatures of these molybdenum-based compounds may unavoidably lead to the agglomeration and coalescence of active species, resulting in a decreased number of exposed active sites.

Constructing molybdenum-based compounds with ideal nanostructures, such as nanotube [15], nanowire [16], and nanosheet [17] can endow their large specific surface area for the full exposure of accessible active sites, abundant open spaces/nanopores for mass

* Corresponding authors.

** Corresponding author at: School of Chemistry and Chemical Engineering & Inner Mongolia Engineering and Technology Research Center for Catalytic Conversion and Utilization of Carbon Resource Molecules, Inner Mongolia University, 49 Xilingoule South Road, Hohhot 010020, PR China.

E-mail addresses: cebliu@imu.edu.cn (B. Liu), gaorui@imu.edu.cn (R. Gao), cejzhang@imu.edu.cn (J. Zhang).

transfer, and good electrical conductivity for electron transfer during HER, and thereby resulting an enhanced HER performance. Among various nanostructures, two-dimensional nanosheet with a large specific surface area, sufficient open nanopores/spaces, and abundant edge sites is beneficial to the exposure of superficial active sites and electron/mass transfer and has received special attention [18–21]. In addition, the nanosheet can be *in situ* grown on the current collector to form a self-supported monolithic electrode, which ensures good electrical contact and strong adhesive strength between the active species and the current collector, meanwhile, provides abundant active sites and sufficient spaces for electron transfer and ion diffusion, thus obtaining an enhanced electrocatalytic performance [22–24]. Up to date, many molybdenum-based compounds nanosheets, such as NPSCL@S-MoP [18], MoP/MoO₂ [19], MoS₂/Mo₂C [20], and MoP/MoS₂ [21] nanosheets have been exploited via various synthetic methods. However, it is still lack of universal methods to fabricate nanosheets of various molybdenum-based compounds.

Apart from tuning the structure, anions (N, P, and/or S) doping is another efficient approach to induce superior HER performance of molybdenum-based catalysts [18]. Among these dopants, nonmetal S is one of the effective dopants and is widely applied [18,25]. The introduction of S in the lattice of molybdenum-based compounds can modulate their electronic structures and elevate the reaction kinetics directly, resulting in its working as alien catalytic sites [25,26]. Nevertheless, the introduction of dopants commonly requires methods of post-treatment and it is time-consuming and tedious. The simultaneous *in situ* introduction during the synthesis of molybdenum-based compounds is an ideal way, but is still rarely reported.

In this work, we construct self-standing monolithic electrodes consisting of ultrathin sulfur-doped molybdenum-based compounds (S-Mo₂C, S-MoP, S-MoN, and S-MoO₃) nanosheets derived from MoS₂ ultrathin nanosheets on carbon cloth (labeled as S-Mo₂C/CC, S-MoP/CC, S-MoN/CC, and S-MoO₃/CC) via *in situ* topological transformation method to boost the HER performance. During the high-temperature phase transformation process, the MoS₂ nanosheets not only supply molybdenum source, but also release sulfur species and are *in situ* doped in the obtained molybdenum-based compounds. The well-defined porous nanosheet structure accommodates abundant exposed active sites, enhances electronic conductivity, and provides sufficient spaces for mass/charge transfer, and thereby promoting interfacial electrocatalytic reactions. More importantly, experimental and theoretical calculations results reveal that the synergistic effect between S dopant and MoX_n induces an optimized electronic state of S-MoX_n, thus resulting in energy-favorable proton adsorption and hydrogen desorption behaviors over the S-MoX_n surface. Accordingly, the 2D S-MoX_n/CC shows an enhanced HER activity compared to MoX_n/CC. Remarkably, the optimized S-MoP/CC electrode exhibits low overpotentials of 75, 75, and 127 mV at 10 mA cm⁻² in acidic, alkaline, and neutral media, respectively and could maintain a stable performance in 30 h continuous operation. This study presents a feasible and universal route to construct the sulfur-doped molybdenum-based compounds catalysts for various electrocatalytic applications and offers a prospective insight to synthesize various electrocatalysts well-defined nanostructures.

2. Experimental section

2.1. Electrode preparation

2.1.1. Preparation of MoS₂/CC and MoO₃/CC

The carbon cloth was refluxed with concentrated nitric acid at 80 °C for 12 h and washed with distilled water, ethanol, and acetone for 20 min, respectively. MoS₂/CC and MoO₃/CC were prepared via a modified hydrothermal method [16,27]. To obtain MoS₂/CC, sodium molybdate dihydrate (Na₂MoO₄·2H₂O, 0.54 g) and thiourea (CH₄N₂S, 0.18 g) were dissolved in distilled water (32 mL) under stirring. The solution was transferred into a Teflon-lined stainless autoclave (50 mL) and a piece of

carbon cloth (3 cm × 2 cm) was immersed into the solution. After maintaining 220 °C for 24 h, the autoclave was cooled down to room temperature. The synthesized product was rinsed with deionized water and ethanol before being dried at 60 °C under a vacuum to obtain MoS₂/CC. To achieve MoO₃/CC, ammonium molybdate (0.98 g) and tartaric acid (0.24 g) were first dissolved in deionized water (35 mL), and the pH value of the solution was adjusted to about 1.0 with 3.0 M nitric acid. Then, the mixture solution was transferred to a 50 mL autoclave for hydrothermal reaction at 160 °C for 5 h. After cooling to room temperature, the CC was taken out and cleaned with deionized water and ethanol, then dried at 60 °C for 2 h to obtain MoO₃/CC.

2.1.2. Preparation of S-Mo₂C/CC and Mo₂C/CC

A piece of obtained MoS₂/CC was placed in a tube furnace and heated to 850 °C for 3 h at a heating ramp of 2 °C min⁻¹ in a 20 % H₂/CH₄ atmosphere with a flow rate of 50 mL·min⁻¹. After cooling to room temperature and passivating using a 0.5 % O₂/Ar gas mixture, the S-Mo₂C/CC was obtained. The Mo₂C/CC was prepared using the same synthesis method except for replacing MoS₂/CC with MoO₃/CC.

2.1.3. Preparation of S-MoP/CC and MoP/CC

A piece of obtained MoS₂/CC was placed in a quartz boat with 1.0 g of NaH₂PO₂·H₂O at the upstream side of the furnace, and then the furnace was heated to 850 °C for 3 h at a heating ramp of 10 °C min⁻¹ in N₂ atmosphere. After cooling to room temperature, the S-MoP/CC was obtained. The MoP/CC was prepared using the same synthesis method except for replacing MoS₂/CC with MoO₃/CC.

2.1.4. Preparation of S-MoN/CC and MoN/CC

A piece of obtained MoS₂/CC was placed in a tube furnace, and then the furnace was heated to 750 °C for 3 h at a heating ramp of 2 °C min⁻¹ in an NH₃ atmosphere with a flow rate of 100 mL·min⁻¹. After cooling to room temperature, the S-MoN/CC was achieved. The MoN/CC was prepared using the same synthesis method except for replacing MoS₂/CC with MoO₃/CC.

2.1.5. Preparation of S-MoO₃/CC

A piece of obtained MoS₂/CC was placed in a tube furnace and then the furnace was heated to 350 °C for 2 h at a heating rate of 2 °C min⁻¹ in air. After cooling to room temperature, the S-MoO₃/CC was obtained.

2.1.6. Preparation of Pt/C/CC

For comparison, Pt/C/CC was prepared by using Pt/C(20 %) loading on CC (carbon cloth). Typically, 40 mg Pt/C(20 %) was dispersed in a mixed solution of deionized water (160 μL), ethanol (200 μL), and Nafion (40 μL, D-521 dispersion, 5 % w/w in water) and ultrasonicated for 20 min. After a piece of CC (1 cm × 1 cm) was placed in the mixture and soaked for 2 h, the CC was transferred to a vacuum oven and dried at 80 °C for 4 h. We repeated this process until the mass loading of Pt/C reached ~3.0 mg cm⁻², which is close to the loading amount of S-MoX_n on the S-MoX_n/CC.

2.2. Electrode characterization

The S-MoX_n/CC electrodes were characterized by X-ray powder diffraction (XRD, PANalytical Empyrean), transmission electron microscopy and scanning transmission electron microscopy equipped with energy-dispersive X-ray (EDX) spectrometer (TEM and STEM, FEI Tecnai F20), scanning electron microscopy equipped with EDX spectrometer (SEM, Hitachi S-4800), X-ray photoelectron spectroscopy (XPS, Thermo Scientific ESCALAB Xi⁺), and Raman spectra (Renishaw, laser wavelength 532 nm). To prepare the samples for TEM, STEM, and EDX measurements, the catalysts (S-MoX_n) were first scraped down from the carbon cloth substrate, and then were uniformly dispersed in absolute ethanol in a centrifuge tube by ultrasonic treatment for 10 min.

2.3. Electrochemical measurements

The electrochemical measurements were carried out on an electrochemical workstation (CHI 760E) in a conventional three-electrode system, with a carbon rod electrode as the counter electrode, the as-prepared catalysts as the working electrode, and a saturated calomel electrode (SCE, 0.241 V vs. RHE) as the reference electrode. All potentials were referred to a reversible hydrogen electrode (RHE) according to $E_{RHE} = E_{SCE} + E_{SCE}^0 + 0.059 \times pH$. The linear-sweep voltammetry (LSV) tests were conducted in 0.5 M H₂SO₄, 1.0 M KOH, and 1.0 M PBS electrolytes at a scan rate of 2 mV s⁻¹ after 30 cycles of cyclic voltammetry (CV) scan. The accelerated durability tests (ADTs) for 5000 CV cycles were conducted in 0.5 M H₂SO₄ media (purged with pure N₂) to assess the HER durability. The long-term stability of catalysts was evaluated by amperometric current density-time (i-t) measurements at a constant potential which was obtained according to LSV curves at 100 mA cm⁻² in 0.5 M H₂SO₄ and 1.0 M KOH electrolytes, as well as 50 mA cm⁻² in 1.0 M PBS electrolyte. Electrochemical impedance spectroscopy (EIS) was carried out in the frequency range from 100 kHz to 0.1 Hz with an AC amplitude of 10 mV.

2.4. Computation details

2.4.1. DFT methods

All spin-polarized first principle calculations were performed using the Vienna Ab Initio Simulation Package (VASP) [28]. The projector augmented wave (PAW) method was applied to describe the electron-ion interaction [29], and Perdew-Burke-Ernzerhof (PBE) was adopted for the electron exchange and correlation energies [30]. The cutoff of the plane wave was set as 450 eV, and MP k-point sampling was used and all of the calculations were converged to the energy change of 1×10^{-5} . The free energies were evaluated by $\Delta G_{(H^*)} = \Delta E_{(H^*)} + \Delta ZPE - T\Delta S$, where $\Delta E_{(H^*)}$ is the total reaction energy change calculated using DFT calculations, ΔZPE is the correction in zero-point energy, T is the temperature (298.15 K), and the ΔS is the change in entropy, which values is calculated for the absorbed species using harmonic vibrational frequency analysis. For the zero-point energy correction, both the gaseous molecule of H₂ (0.27 eV) and adsorbed H atom on the models of MoS₂(002) (0.22 eV), Mo₂C(101) (0.19 eV), S-Mo₂C(101) (0.19 eV), MoP(100) (0.17 eV), S-MoP(100) (0.14 eV), S-MoN(202) (0.20 eV), and S-MoO₃(010) (0.23 eV) have been considered. Additionally, the free energy of one H^{*} was calculated by $G_{H^*} = 1/2G_{H2}$.

2.4.2. Models

The calculated lattice constant of MoS₂ cell is $a = b = 3.191 \text{ \AA}$, $c = 14.605 \text{ \AA}$, $\alpha = \beta = 90^\circ$, $\gamma = 120^\circ$; the lattice constants of Mo₂C unit cell is $a = b = c = 3.057 \text{ \AA}$, $\alpha = \beta = 90.00^\circ$, $\gamma = 120.00^\circ$; the lattice constants of MoP unit cell is $a = b = c = 3.239 \text{ \AA}$, $\alpha = \beta = 90.00^\circ$, and $\gamma = 120.00^\circ$; the lattice constants of MoN unit cell is $a = b = 5.764 \text{ \AA}$, $c = 5.685 \text{ \AA}$, $\alpha = \beta = 90.00^\circ$, and $\gamma = 120.00^\circ$; the lattice constants of MoO₃ unit cell is $a = 3.964 \text{ \AA}$, $b = 14.244 \text{ \AA}$, $c = 3.716 \text{ \AA}$, $\alpha = \beta = \gamma = 90.00^\circ$. The seven catalyst models of MoS₂(002), Mo₂C(101), S-Mo₂C(101), MoP(100), S-MoP(100), S-MoN(202), and S-MoO₃(010) were constructed. All of the models were constructed with a vacuum slab of 15 Å in the z-direction. Totally, MoS₂(002) has 48 S and 24 Mo atoms; Mo₂C(101) has 24 C and 48 Mo atoms, in which 8 C and 16 Mo atoms are fixed; S-Mo₂C(101) has 23 C, 1 S, and 48 Mo atoms, in which 8 C and 16 Mo atoms are fixed; MoP(100) has 48 P and 48 Mo atoms, in which 16 P and 16 Mo atoms are fixed; S-MoP(100) has 47 P, 1 S, and 48 Mo atoms, in which 16 P and 16 Mo atoms are fixed; S-MoN(202) has 39 N, 1 S, and 40 Mo atoms, in which 16 N and 16 Mo atoms are fixed; S-MoO₃(010) has 35 O, 1 S, and 12 Mo atoms, in which 12 O and 6 Mo atoms are fixed.

3. Results and discussion

3.1. Design and fabrication strategy of self-supported S-MoX_n/CC electrodes

The self-supported S-MoX_n/CC electrodes (S-MoP/CC, S-Mo₂C/CC, S-MoN/CC, and S-MoO₃/CC) were fabricated via a two-step synthetic strategy (Fig. 1). First, the MoS₂ nanosheets grown on carbon cloth (MoS₂/CC) was synthesized by a hydrothermal method. After that, the MoS₂/CC precursor was subjected to a phosphidation treatment using the NaH₂PO₂ as a P source, a carbonization treatment in the CH₄ atmosphere, a nitridation treatment in NH₃ flow, and an oxidation process in the air to obtain S-MoP/CC, S-Mo₂C/CC, S-MoN/CC, and S-MoO₃/CC electrodes, respectively. The 3D self-supported binder-free monolithic structure assembled from 2D ultrathin S-MoX_n nanosheets on CC ensures good electrical contact between the catalyst and the substrate electrode, abundant active sites, sufficient spaces for electron transfer and ion diffusion, and structural stability, thereby improving the HER performance [22–24]. For comparison, the MoP/CC, Mo₂C/CC, MoN/CC, and MoO₃/CC electrodes were also synthesized via a similar approach except for using the MoO₃/CC as the precursor. The experimental details are displayed in the section of electrode preparation.

3.2. Phases, morphology, and structure of self-supported S-MoX_n/CC electrodes

X-ray powder diffraction (XRD) analysis was performed to identify the crystalline phase of various S-MoX_n/CC electrodes derived from MoS₂/CC precursor (Fig. 2a). The MoS₂/CC shows four obvious characteristic peaks at 14.4°, 32.7°, 39.5°, and 49.8°, being indexed to the (002), (100), (103), and (105) lattice planes of MoS₂ (PDF#37-1492). The diffraction peaks of S-MoP/CC locate at 27.9°, 32.2°, 43.1°, and 57.5°, which correspond well to the (002), (100), (103), and (105) planes of hexagonal MoP (PDF#24-0771), demonstrating the full conversion of MoS₂ into MoP after phosphatization reaction. Meanwhile, the XRD patterns of S-Mo₂C/CC, S-MoN/CC, and S-MoO₃/CC display the characteristic diffraction peaks of hexagonal Mo₂C (PDF#35-0787), hexagonal MoN (PDF#89-2904), and orthorhombic MoO₃ (PDF#05-0508), respectively, implying that the MoS₂ has been converted to Mo₂C, MoN, and MoO₃, respectively. Furthermore, although the S-MoX_n/CC electrodes were prepared at high temperatures, the grain sizes of MoN, Mo₂C, MoP, and MoO₃ nanoparticles in S-MoN/CC, S-Mo₂C/CC, S-MoP/CC, and S-MoO₃/CC electrodes calculated using Scherrer equation are about 15.2, 15.3, 17.8, and 19.8 nm, respectively, still lower than 20 nm, implying that the ultrathin MoS₂ nanosheet precursor can effectively refine the grain of MoX_n.

To further reveal the chemical structure and composition information, the Raman spectra of S-MoX_n/CC derived from MoS₂/CC were recorded and analyzed (Fig. 2b). The MoS₂/CC presents two peaks located at wavenumbers of 406 cm⁻¹ and 380 cm⁻¹, corresponding to the vibration modes of in-plane E_{2g}¹ and out-of-plane A_{1g}, in which the peak separation (Δk) is 26.5 cm⁻¹, implying the formation of multi-layered MoS₂ nanosheets [31,32]. The Raman peaks of S-Mo₂C/CC at 1346 cm⁻¹, 1572 cm⁻¹, and 2688 cm⁻¹ are related to defective sp³-carbon (D band), conductive sp²-carbon (G band), and ordered layer carbon (2D-band) in surface carbon layer [33]. Interestingly, the intensity ratio of D to G bands (I_D/I_G) is calculated to be a high value of 1.74, suggesting that the existence of numerous partial graphitization and disordered structures could provide electrocatalytic active sites for promoting the proton/hydrogen desorption [34,35]. The narrow characteristic peak appearing at 408 cm⁻¹ for S-MoP/CC indicates the complete formation of crystalline MoP derived from the pristine MoS₂ [36]. It is noted that the location of Raman peaks for S-MoN/CC is same as that of S-MoO₃/CC except for the lower intensity, which may be because the MoN surface is easy to be oxidized to MoO_x in the air [37, 38].

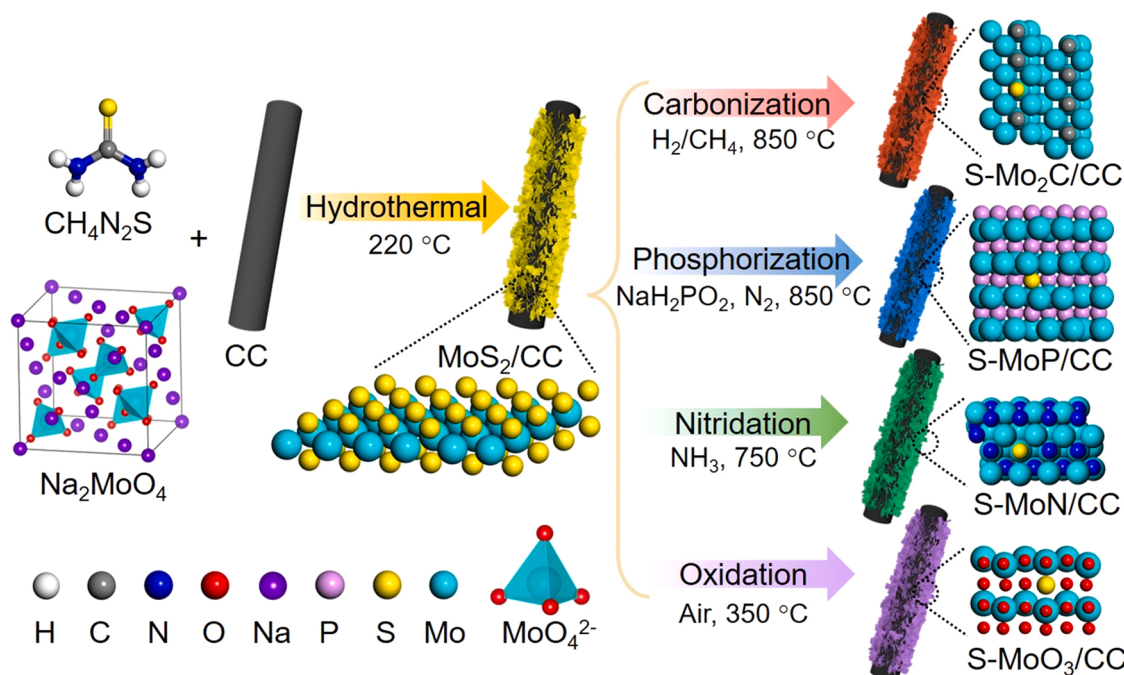


Fig. 1. Schematic illustration of the preparation of S-MoX_n/CC electrodes.

Scanning electron microscopy (SEM) characterization was carried out to reveal the morphology and structure of the S-MoX_n/CC electrodes. The bare CC is composed of carbon fiber with a smooth surface (Fig. 2c). Low-magnification SEM images of MoS₂/CC and S-MoX_n/CC electrodes show that the MoS₂ and S-MoX_n consist of interconnected nanosheets with open and porous morphology are tightly grew on carbon fiber (Fig. 2d, f, h, j, and l). High-magnification SEM images display that the MoS₂ and S-MoX_n have different microstructures. For MoS₂/CC precursor, the cross-linked smooth MoS₂ nanosheets with a lateral size of several micrometers and a thickness of \approx 15 nm are vertically grown on each fiber of CC (Fig. 2e). After topotactic transformations under different reaction atmospheres, the obtained S-Mo₂C and S-MoN on CC show porous nanosheet-like morphology at overall, and which is composed of the interconnected, irregular, and smaller S-Mo₂C and S-MoN nanosheets in microcosmic (Fig. 2g, k). While, the obtained S-MoP and S-MoO₃ on CC are composed of linked and stacked nanosheets (Fig. 2i, m). Compared to MoS₂ nanosheets, the thickness of obtained MoX_n nanosheets has increased of varying degrees, and follows the order of S-MoO₃ (\approx 35 nm) $>$ S-MoP (\approx 30 nm) $>$ S-Mo₂C (\approx 25 nm) \approx S-MoN (\approx 25 nm) due to the Ostwald ripening during high-temperature treatment, consistent with the XRD results [39]. Energy-dispersive X-ray (EDX) spectrum shows that a small amount of S element still presents in the S-Mo₂C/CC, S-MoP/CC, S-MoN/CC, as well as S-MoO₃/CC even after thermal treatment (Figs. S1–S5), confirming the successful doping of S species in S-MoX_n/CC. Additionally, the EDX elemental mapping images show the corresponding elements uniformly disperse in S-MoX_n/CC, further verifying the successful fabrication of S-MoX_n/CC derived from MoS₂/CC.

The morphology and nanostructure of MoS₂, S-Mo₂C, S-MoP, S-MoN, and S-MoO₃ nanosheets scraped down from CC substrate were further explored by transmission electron microscopy (TEM) images (Fig. 3a, c, f, i, k). The TEM image shows that the irregular and unbroken nanosheets with length and width of few micrometers and thickness of about 20 nm are observed in MoS₂ precursor (Fig. 3a). The high-resolution TEM (HRTEM) image clearly displays the lattice fringes with distances of 0.616 and 0.228 nm simultaneously, which are assigned to the (002) and (103) planes of MoS₂ (Fig. 3b). After carbonization, the nanosheets were shattered into stacked pieces with rich nanopores (Fig. 3c).

Meanwhile, the lattice fringes with spacings of 0.229 and 0.237 nm, corresponding to the (101) and (002) lattice planes of Mo₂C, respectively, can be found, which further confirms the successful synthesis of hexagonal Mo₂C (Fig. 3d). The STEM image and corresponding EDX mapping images (Fig. 3e) display that the broken S-Mo₂C nanosheets stack each other and links together with the uniformly distribution of Mo, C, S elements over the whole S-Mo₂C nanosheets, further suggesting the successful doping of S in the Mo₂C nanosheets. Additionally, EDX spectrum analysis of the obtained S-Mo₂C reveals that the atomic percentage of the S atoms is approximately 0.73 at% (Fig. S6), which agrees well with the foregoing SEM-EDX result (0.82 at%, Fig. S2). After phosphidation, the irregular, partial sintered, and cross-linked S-MoP nanosheets with length in about 200 nm were obtained (Fig. 3f). The HRTEM image of S-MoP exhibits the lattice fringes with an interplanar spacing of 0.278 nm assignable to the (100) facet of hexagonal MoP (Fig. 3g), confirming the realization of MoP. The atomic percentage of the S element in S-MoP is quantified to be about 6.37 at% by the EDX spectrum (Fig. S7), close to the value determined by the SEM-EDX spectrum (6.75 at%), indicating the even dispersion of S species in S-MoP nanosheets. The EDX elemental mappings further confirm that the S-MoP nanosheets consist of Mo, P, and S, and each element uniformly runs throughout the nanosheets (Fig. 3h). In addition, the S-MoN is composed of stacked and linked nanosheets with a thickness of 25 nm and forms abundant nanopores among nanosheets (Fig. 3i). Meanwhile, the lattice fringes with distances of 0.183 and 0.245 nm assignable to the (202) and (200) planes of MoN are observed in the HRTEM image (Fig. 3j). Similarly, the S-MoO₃ also consists of cross-linked and small-sized S-MoO₃ pieces (Fig. 3k) meanwhile the fringes with distances of 0.213 and 0.381 nm corresponding to the (141) and (110) planes of MoO₃ are found (Fig. 3l). The above HRTEM results indicate the formation of targeted crystalline structure, consistent with the XRD results.

The nitrogen adsorption-desorption isotherms of S-MoX_n and MoS₂ display that the S-Mo₂C, S-MoN, and S-MoP show type IV isotherms with H3 type hysteresis loops, the S-MoO₃ displays a type IV isotherm with a H2 type hysteresis loop, and no obvious hysteresis loop can be found in MoS₂, suggesting the mesoporous nature of S-MoX_n (Fig. S8a). The Brunauer-Emmett-Teller (BET) surface area of S-Mo₂C and S-MoN are calculated to be 75.8 m² g⁻¹ and 84.1 m² g⁻¹, larger than that of S-MoP

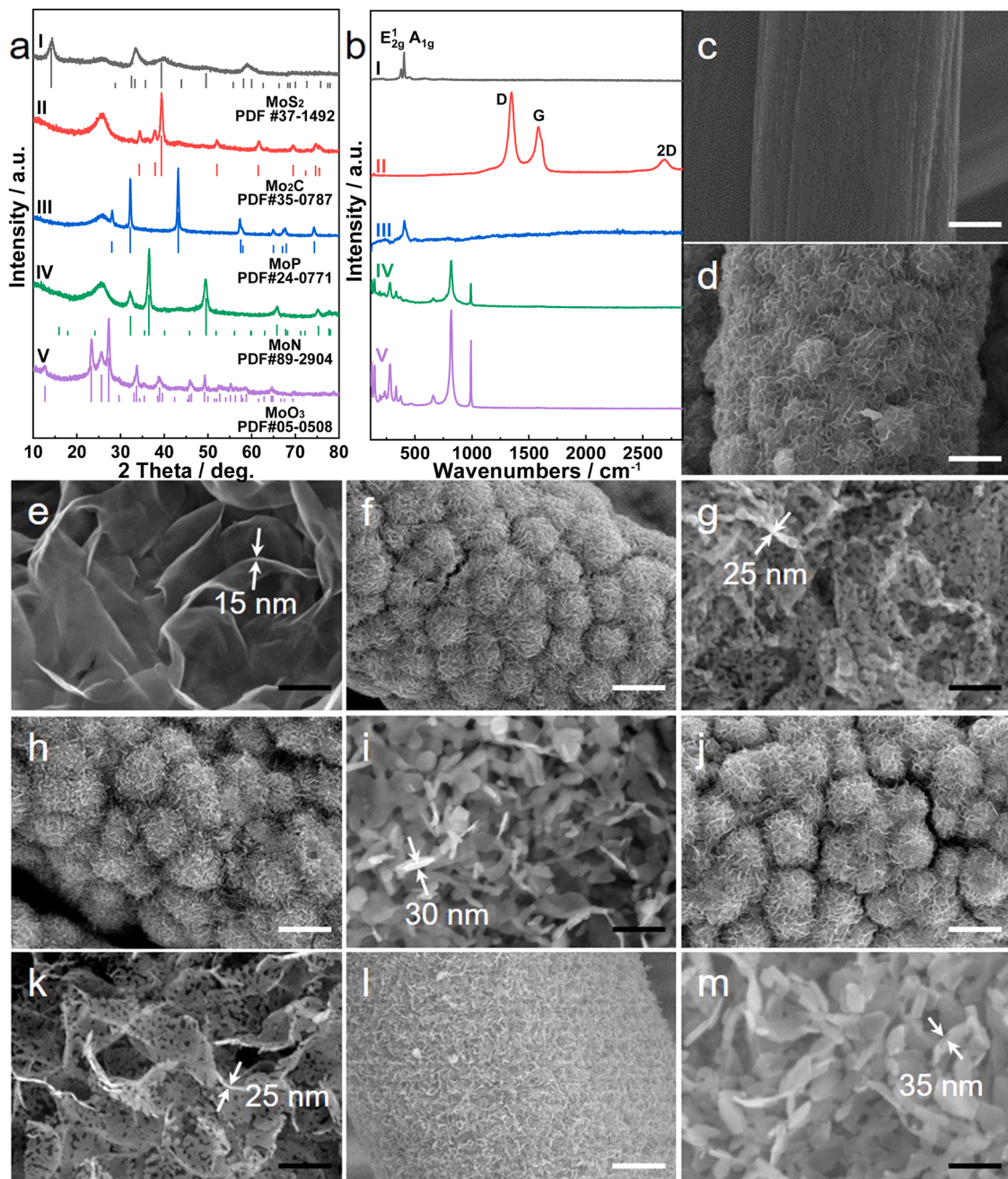


Fig. 2. (a) XRD patterns and (b) Raman spectra of (I) MoS₂/CC, (II) S-Mo₂C/CC, (III) S-MoP/CC, (IV) S-MoN/CC, and (V) S-MoO₃/CC. SEM images of (c) CC, (d, e) MoS₂/CC, (f, g) S-Mo₂C/CC, (h, i) S-MoP/CC, (j, k) S-MoN/CC, (l, m) S-MoO₃/CC. The white and black scale bars in SEM images represent 2 μ m and 200 nm, respectively.

(64.9 $\text{m}^2 \text{ g}^{-1}$), MoS₂ (53.5 $\text{m}^2 \text{ g}^{-1}$), and S-MoO₃ (37.2 $\text{m}^2 \text{ g}^{-1}$). The corresponding Barrett-Joyner-Halenda (BJH) pore size distribution curves (Fig. S8b) show that the average pore size of S-Mo₂C, S-MoP, S-MoN, and S-MoO₃ are 2.5, 2.8, 3.5, and 2.0 nm, respectively while no obvious mesopores distribution can be observed in MoS₂. Meanwhile, it is seen that the mesopores existed in S-Mo₂C and S-MoN are more than that in S-MoP and S-MoO₃. The high surface area with plentiful mesopores may facilitate the exposure of active sites and efficiently promotes electrolyte diffusion and charge transfer [35], thus resulting in an enhanced activity for HER.

3.3. Surface composition and valence states of self-supported S-MoX_n/CC electrodes

The surface composition and valence states of the S-MoX_n/CC were elucidated by X-ray photoelectron spectroscopy (XPS) measurements. In the high-resolution Mo 3d XPS spectra of the S-MoX_n/CC and MoX_n/CC (Fig. 4a), the peaks at binding energies (B.E.) of 231.4–231.9 and 228.3–228.8 eV are ascribed to 3d_{3/2} and 3d_{5/2} orbits of Mo^{δ+}. Other two doublets in the binding energy region of 232.0–232.5/228.9–229.4 eV (Mo⁴⁺ 3d_{3/2} and Mo⁴⁺ 3d_{5/2}) and 235.4–235.8/232.6–233.1 eV (Mo⁶⁺ 3d_{3/2} and Mo⁶⁺ 3d_{5/2}) are assigned to high oxidation states of Mo species due to the surface oxidation. Notably, the binding energies of Mo^{δ+} 3d_{5/2} in S-Mo₂C/CC and S-MoP/CC exhibit positive shifts of about 0.10 and 0.25 eV compared to that in Mo₂C/CC

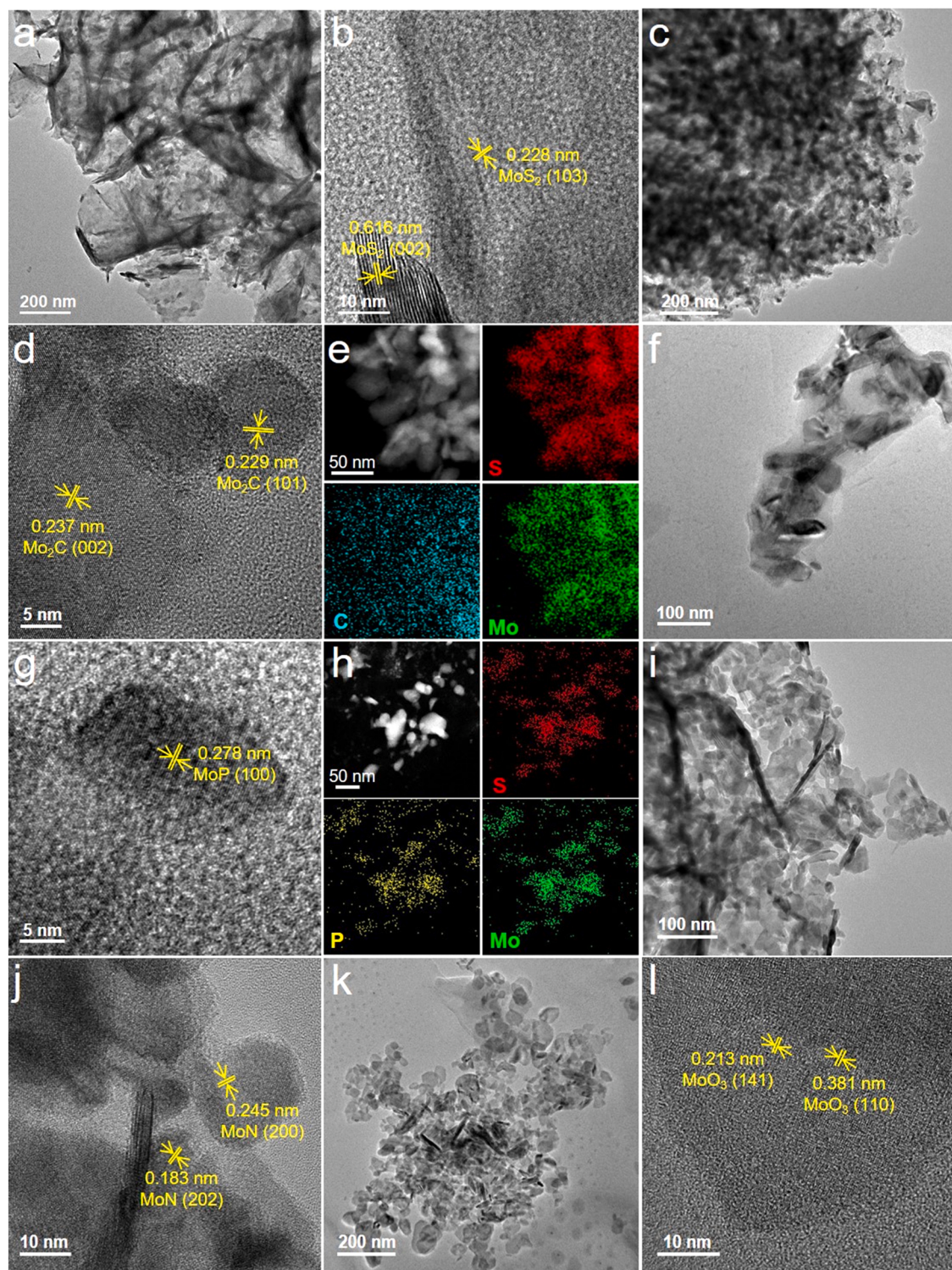


Fig. 3. TEM and HRTEM images of (a, b) MoS₂, (c, d) S-Mo₂C, (f, g) S-MoP, (i, j) S-MoN, and (k, l) S-MoO₃. STEM images and the corresponding elemental mapping images of (e) S-Mo₂C and (h) S-MoP.

and MoP/CC, while negative shifts of -0.15 and -0.20 eV can be observed in S-MoN/CC and S-MoO₃/CC compared to that of MoN/CC and MoO₃/CC. Conversely, the binding energies of P 2p peaks in S-MoP exhibit a positive shift of 0.20 eV compared to those peaks in MoP, while the negative shifts of -0.15 and -0.25 eV for N 1s peaks in S-MoN and O 1s peaks in S-MoO₃ can be found compared to that in MoN and MoO₃ (Fig. 4b). These results provide the evidence of strong electronic interaction between the dopant S and MoX_n in S-MoX_n and suggest the more

electrons transfer from Mo to S in S-MoP and S-Mo₂C and fewer electrons transfer from Mo to S in S-MoN and S-MoO₃, which may optimize the electron density around the Mo atoms in S-MoX_n/CC and results in an enhanced electrocatalytic performance of S-MoX_n/CC [25].

In the S 2p XPS spectra of MoS₂/CC and S-MoX_n/CC (Fig. 4c), the peaks at binding energies of 161.5 – 162.1 eV and 162.8 – 163.3 eV are assigned to S²⁻ bounded to Mo⁴⁺. Notably, the intensity of S 2p peaks in S-MoX_n is significantly weakened and shows obvious shifts of -0.1 eV

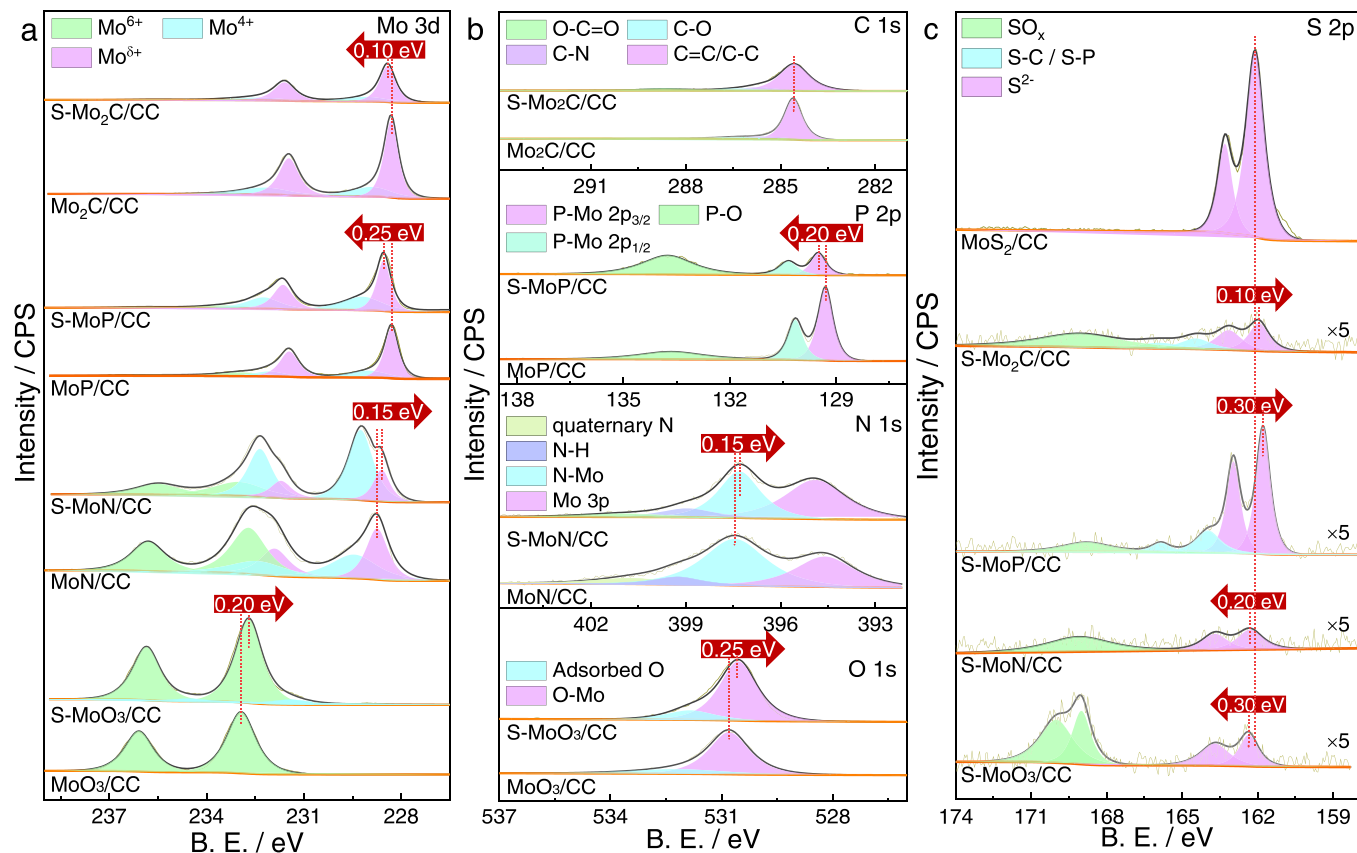


Fig. 4. High-resolution XPS spectra of (a) Mo 3d, (b) C 1s, P 2p, N 1s, and O 1s in S-MoX_n/CC and MoX_n/CC; (c) S 2p in MoS₂/CC and S-MoX_n/CC.

for S-Mo₂C, -0.3 eV for S-MoP, $+0.2$ eV for S-MoN, and $+0.3$ eV for S-MoO₃ in comparison with those peaks in the MoS₂/CC, indicating the occurrence of electronic coupling interactions among Mo, S, and X (X = C, P, N, and O) atoms in the S-MoX_n. The difference of valence states for S in S-MoX_n may be ascribed to the Pauling electronegativity order of O > N > S > C > P. The peaks at the binding energies of 164.2–164.5 eV and 165.8–165.9 eV for S-Mo₂C/CC and S-MoP/CC are attributed to C-S and C-P species, further suggesting the successful doping of S in the lattice of Mo₂C and MoP. In addition, the peaks at the binding energies of 168.7–170.0 eV correspond to SO_x species deriving from the surface oxidation of S-MoX_n [31]. These results imply that the doped S can modulate the surface electron states of S-MoX_n, which may facilitate to optimize the electron structure of S-MoX_n, thereby enhancing the HER activity [25].

3.4. Electrochemical performance

The electrocatalytic HER performance of the MoS₂/CC, S-Mo₂C/CC, S-MoP/CC, S-MoN/CC, S-MoO₃/CC, and commercial 20 wt% Pt/C catalyst were investigated with iR correction using a standard three-electrode setup in N₂-saturated 0.5 M H₂SO₄ solution (pH = 0.3). The linear scan voltammetry (LSV) curves are shown in Fig. 5a. Obviously, the Pt/C catalyst exhibits a preeminent HER activity with an overpotential of 35 mV at a cathodic current density of 10 mA cm⁻² (η_{10}), while the S-MoN and S-MoO₃ electrodes display poor HER activities with high η_{10} of 259 and 344 mV resulting from the inferior intrinsic activities of MoN and MoO₃ for HER [5]. The η_{10} values of S-MoP/CC and S-Mo₂C/CC are 75 mV and 98 mV, respectively, lower than that of MoS₂/CC (123 mV), implying the superior HER activities of S-MoP and S-Mo₂C.

The Tafel plots of the S-MoX_n/CC electrodes were then acquired to further evaluate the intrinsic HER kinetic process (Fig. 5b). The Tafel

slopes of S-MoP/CC, S-Mo₂C/CC, MoS₂/CC, S-MoN/CC, and S-MoO₃/CC electrodes are calculated to be 53.0, 54.6, 79.3, 91.4, and 153.5 mV dec⁻¹, respectively. The Tafel slope values suggest that the HER over S-MoP/CC, S-Mo₂C/CC, MoS₂/CC, and S-MoN/CC electrodes follow the Volmer-Heyrovsky mechanism in acidic medium [25,40,41]. The lower Tafel slopes of S-MoP/CC and S-Mo₂C/CC mean that they have the faster kinetics in HER process. In fact, the HER activity of S-MoP/CC also surpasses most previously reported molybdenum-based noble-metal-free HER electrocatalysts (Fig. 5c and Table S1). To investigate the effect of S doping in S-MoX_n on the HER activity of S-MoX_n/CC, we prepared the S-free electrodes of MoX_n/CC and evaluated their HER activities in 0.5 M H₂SO₄ medium. The recorded LSV curves show that the mass-normalized HER activities of S-MoX_n/CC electrodes are obviously superior to the corresponding MoX_n/CC electrodes (Fig. 5d). To reach a current density of 10 mA mg⁻¹, S-Mo₂C/CC, S-MoP/CC, S-MoN/CC, and S-MoO₃/CC require overpotentials of 124, 99, 301, and 417 mV, superior to that of Mo₂C/CC (179 mV), MoP/CC (152 mV), MoN/CC (315 mV), and MoO₃/CC (448 mV). This result demonstrates that S doping can be used as a facile and effective strategy to enhance the HER activities of MoX_n via the electronic coupling between S and MoX_n [3, 25].

After fitting Nyquist plots of the experimental data using an equivalent circuit (Fig. 5e and Table S2), the charge transfer resistances (R_{ct}) for S-Mo₂C/CC and S-MoP/CC are calculated to be 1.8 and 2.9 Ω , respectively, smaller than that of MoS₂/CC (15.7 Ω), S-MoN/CC (154.8 Ω), and S-MoO₃/CC (229.5 Ω), further demonstrating the faster electron transfer kinetics of S-Mo₂C/CC and S-MoP/CC in the acidic medium during HER. To explore the available active sites during HER, the electrochemically active surface area (ECSA) of MoS₂/CC and S-MoX_n/CC electrodes were evaluated using the double-layer capacitances (C_{dl}) and the average specific capacitance (C_s) (Fig. 5f and Fig. S9) And the value of ECSA was calculated by using ECSA = C_{dl}/C_s, in which C_s

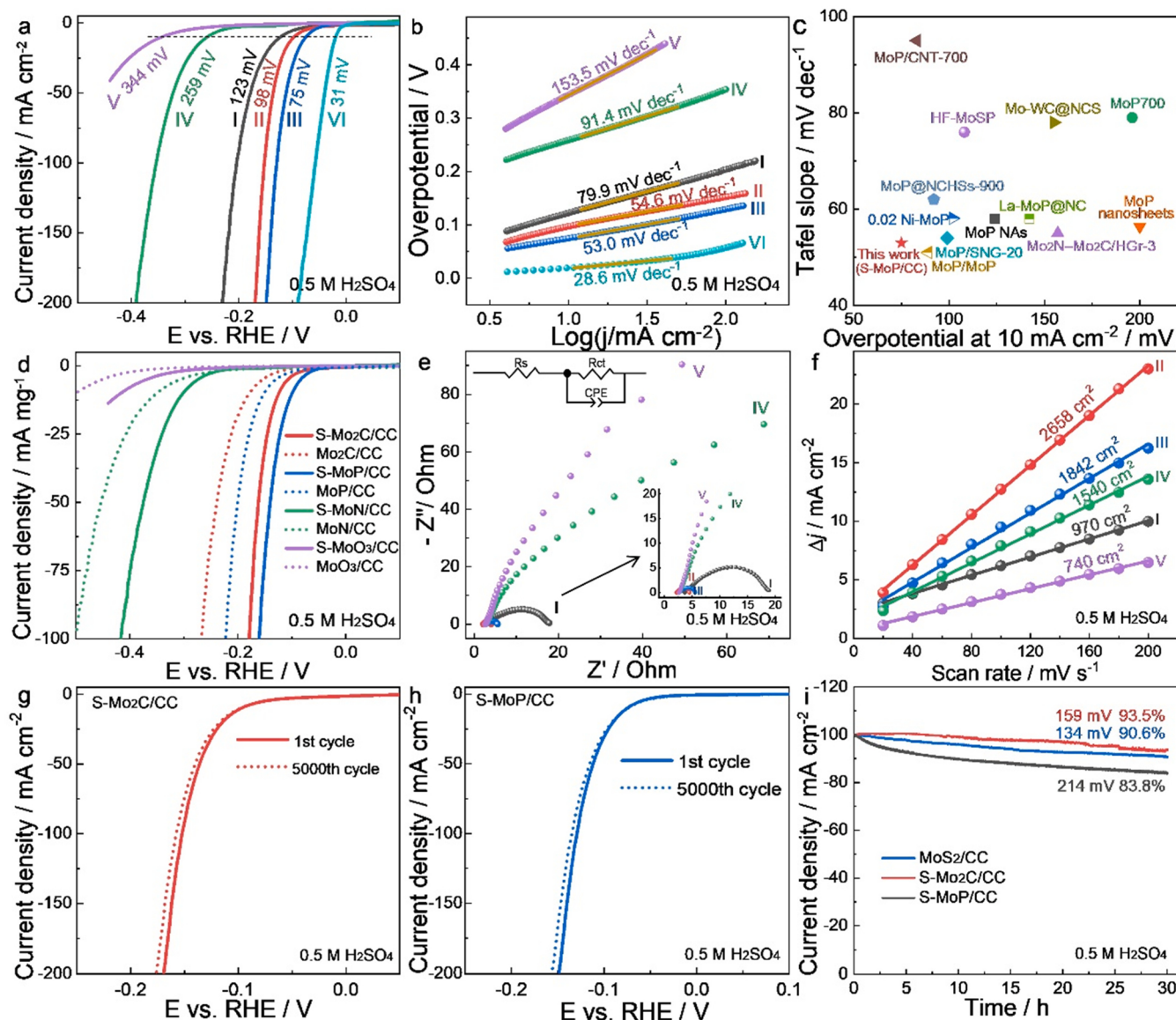


Fig. 5. Electrochemical performance in 0.5 M H₂SO₄ medium. (a) Linear sweep voltammetry curves and (b) Tafel plots of (I) MoS₂/CC, (II) S-Mo₂C/CC, (III) S-MoP/CC, (IV) S-MoN/CC, (V) S-MoO₃/CC, and (VI) Pt/C/CC electrodes. (c) Comparison of the HER performance of S-MoP/CC with the reported molybdenum-based electrocatalysts. (d) Mass-normalized HER activities of S-Mo₂C/CC, Mo₂C/CC, S-MoP/CC, MoP/CC, S-MoN/CC, MoN/CC, S-MoO₃/CC, and MoO₃/CC electrodes (e) Nyquist plots collected at an overpotential of 120 mV, the inset displays one-time-constant model equivalent circuit used for data fitting of EIS spectra; (f) Plots show the ECSA of (I-VI) electrodes at 200 mV vs. RHE. Polarization curves of (g) S-Mo₂C/CC and (h) S-MoP/CC before and after 5000 CV cycles. (i) Chronoamperometry i-t curves of MoS₂/CC, S-Mo₂C/CC, and S-MoP/CC electrodes at different overpotentials to reach a current density of 100 mA cm⁻².

= 40 $\mu\text{F cm}^{-2}$. In this case, the S-Mo₂C/CC presents the largest ECSA of 2658 cm^2 , higher than that of S-MoP/CC (1842 cm^2), Mo₂S/CC (1540 cm^2), S-MoN/CC (970 cm^2), and S-MoO₃/CC (740 cm^2), suggesting that the carbonization and phosphidation treatments can increase the amount of electrochemically active sites while nitridation and oxidation treatments would lead to the decrease numbers of exposed electrochemically active sites. This result shows that the S-Mo₂C/CC has the maximum number of exposed active sites among S-MoX_n/CC electrodes. After normalization by ECSA (Fig. S10), the HER performance of S-MoP/CC is still superior to other catalysts, reflecting its highest intrinsic activity.

Ordinarily, the performance of HER is subject to the following three factors: (1) the intrinsic activity of active sites, (2) the number of active sites, (3) the conductivity of the catalyst [25, 42]. In this work, the S-MoP/CC possesses similar charge-transfer impedance as S-Mo₂C/CC but accommodates a smaller number of active sites than S-Mo₂C/CC, but

its HER activity surpasses S-Mo₂C, which may originate from its superior intrinsic activity. Significantly, a large number of active sites, good conductivity, and high intrinsic activity of S-Mo₂C are plenty enough to accommodate its HER activity superior to Mo₂S/CC, S-MoN/CC, and S-MoO₃/CC electrodes. However, the S-MoN/CC and S-MoO₃/CC electrodes with poor intrinsic activity and inadequate active sites show inferior HER activities to that of Mo₂S/CC.

The durability of S-MoP/CC, S-Mo₂C, and Mo₂S/CC electrodes are further evaluated by accelerated durability tests (ADTs) and amperometric current density-time (i-t) measurements in acidic electrolyte. After 5000 continuous CV cycles, the polarization curves of S-MoP/CC and S-Mo₂C exhibit negligible deterioration in cathodic current density (Fig. 5g, h). In parallel, after a 30 h of continuous electrolysis at a large current density of 100 mA cm⁻² at different overpotentials (Fig. 5i), the S-MoP/CC and S-Mo₂C electrodes can maintain high relative current densities of 90.6 % and 93.5 %, respectively, superior to that of Mo₂S/CC.

CC (83.8 %), further corroborating their good HER stability in acidic electrolyte. In addition, the S-Mo₂C/CC and S-MoP/CC after durability test in acidic medium were characterized by XRD, SEM, SEM-EDX, TEM, HRTEM, and XPS techniques. Notably, the crystalline phase, nanosheet morphology, structure, and elemental composition of the S-Mo₂C/CC and S-MoP/CC electrodes are well remained after durability measurement in acidic media, further demonstrating their good structural and electrocatalytic stability (Figs. S11–S14). Meanwhile, after electrolysis, the binding energies of Mo 3d in the used MoS₂/CC, S-Mo₂C/CC, and S-MoP/CC electrodes occur negative shifts compared to the fresh ones (Fig. S15), which may arise from the depth reduction of MoS₂, S-Mo₂C, and S-MoP during the HER process.

Besides, the electrochemical performance of MoS₂/CC and S-MoX_n/CC in alkaline (1.0 M KOH, pH = 13.8) and neutral (1.0 M PBS, pH = 7) solutions were also assessed (Fig. 6, Figs. S16 and S17). As depicted in Fig. 6a, d, and Table S1, the S-MoP/CC and S-Mo₂C still exhibit outstanding catalytic performance for HER in alkaline/neutral solutions, requiring low η_{10} values of 75/127 mV and 121/161 mV, respectively,

better than those of MoS₂/CC (144/257 mV), S-MoN/CC (181/294 mV), S-Mo₃O₄/CC (312/516 mV), and most of the reported Mo-based HER electrocatalysts in alkaline and neutral media (Table S1). Noteworthily, the current density of S-MoP/CC at high overpotentials (>130 mV) is even higher than that of Pt/C/CC in 1.0 M KOH, further verifying its excellent HER activity. Correspondingly, the small Tafel slopes of 59.1/67.1 mV dec⁻¹ and 64.7/86.3 mV dec⁻¹ in alkaline/neutral media can be also achieved over the S-MoP/CC and S-Mo₂C/CC, still better than those of MoS₂/CC (64.9/135.3 mV dec⁻¹), S-MoN/CC (69.9/95.4 mV dec⁻¹), and S-Mo₃O₄/CC (97.3/262.9 mV dec⁻¹) (Fig. 6b, e and Table S1). This result implies the faster HER kinetics over S-MoP/CC and S-Mo₂C/CC electrodes. Furthermore, after mass normalization, the S-MoP/CC, S-Mo₂C/CC, S-MoN/CC, and S-Mo₃O₄/CC electrodes show overpotentials of 106/207, 155/307, 213/416, and 400/658 mV at 10 mA mg⁻¹, better than that of MoP/CC (118/253 mV), Mo₂C/CC (168/348 mV), MoN/CC (231/451 mV), and Mo₃O₄/CC (442/681 mV), indicating that the S doping can synergistically enhance the electrocatalytic activities of S-MoP/CC, S-Mo₂C/CC, S-MoN/CC, and S-Mo₃O₄/CC.

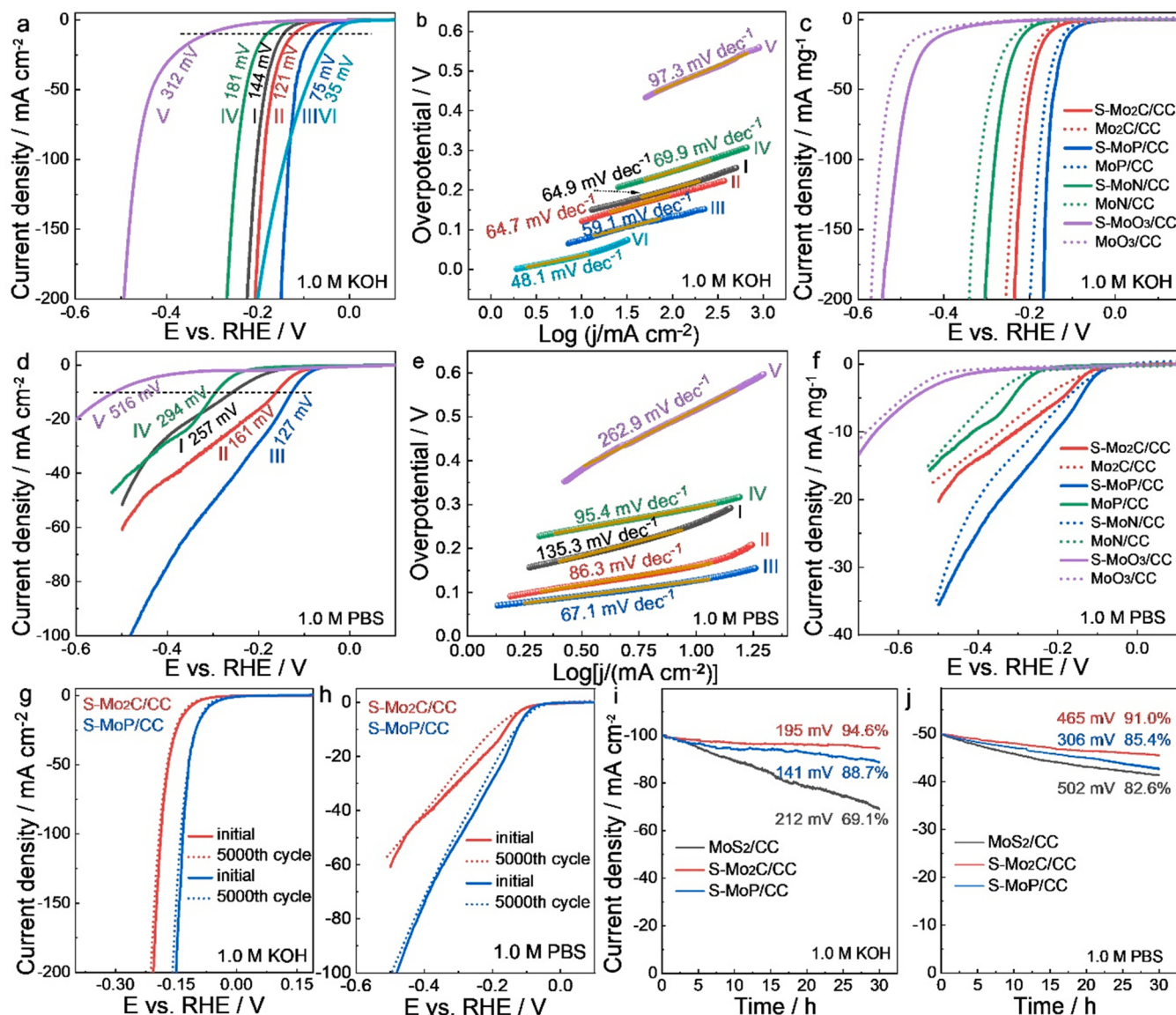


Fig. 6. Electrochemical performance in 1.0 M KOH and 1.0 M PBS solutions (a, d) Polarization curves and (b, e) Tafel plots of (I) MoS₂/CC, (II) S-Mo₂C/CC, (III) S-MoP/CC, (IV) S-MoN/CC, (V) S-Mo₃O₄/CC, and (VI) Pt/C/CC electrodes (g, h) polarization curves of S-Mo₂C/CC and S-MoP/CC before and after 5000 CV cycles; (c, f) Mass-normalized HER activities of S-Mo₂C/CC, Mo₂C/CC, S-MoP/CC, MoP/CC, S-MoN/CC, MoN/CC, S-Mo₃O₄/CC and Mo₃O₄/CC electrodes; (i, j) Chronoamperometry i-t curves of MoS₂/CC, S-Mo₂C/CC, and S-MoP/CC electrodes at fixed overpotentials to reach the current densities of 100 and 50 mA cm⁻².

CC for HER in alkaline and neutral media (Fig. 6c, f). In addition, the S-MoP/CC and S-Mo₂C/CC electrodes also display outstanding long-term stability in both alkaline and neutral media. After 5000 cycles, the decline of current density in the LSV curves of S-Mo₂C and S-MoP/CC is very small (Fig. 6g, h). Meanwhile, after sustaining operation for 30 h at fixed overpotentials (Fig. 6i), the S-Mo₂C/CC and S-MoP/CC electrodes can retain relative current densities of 94.6 %/91.0 % and 88.7 %/85.4 % in alkaline/neutral media, superior to that of MoS₂/CC (69.1 %/82.6 %). This tendency is similar to that in the acid environment, emphasizing the good HER stability of the S-MoP/CC and S-Mo₂C/CC electrodes in pH-universal electrolytes.

3.5. Theoretical calculations

To reveal the intrinsic mechanism of doping S into MoX_n compounds to enhance the HER activity at the atomic level, Density Functional Theory (DFT) calculations were further performed to obtain the information of the adsorption free energy of H* (ΔG_{H^*}) on S-MoX_n catalysts and their electronic structures. The simulated S-doped MoX_n models of S-Mo₂C(101), S-MoP(100), S-MoN(202), S-MoO₃(010), and basal and edge sites of MoS₂, as well as the S-free MoX_n models of Mo₂C(101), MoP(100) MoN(202), and MoO₃(010) for comparison were built (Figs. S18 and S19) based on the XRD and HRTEM results. It is well known that an outstanding HER catalyst accompanies with a thermo-neutral ΔG_{H^*} close to zero. As shown in Fig. 7a, the basal and edge sites of MoS₂ show large endothermic ΔG_{H^*} of 0.95 and 0.77 eV, respectively, suggesting weak adsorption of H* on the basal and edge sites of MoS₂. In contrast, the bare Mo₂C, MoP, MoN, and MoO₃ exhibit large exothermic ΔG_{H^*}

values of -0.68, -0.79, -0.92, and -0.97 eV owing to the strong bonding of Mo-H on their surfaces. After doping S atoms into Mo₂C, MoP, MoN, and MoO₃, the obtained S-Mo₂C, S-MoP, S-MoN, and S-MoO₃ display decreased endothermic ΔG_{H^*} values of -0.55, -0.15, -0.82, and -0.70 eV, closer to zero than those S-free counterparts, implying that the S dopant in MoX_n can promote the HER activity of S-MoX_n [18]. Based on the ΔG_{H^*} values, it is deduced that the order of HER activities should be S-MoP > S-Mo₂C > MoS₂ > S-MoN > S-MoO₃ in theory, which agrees well with the experimental results.

To gain a further insight into the catalytic HER mechanism, we also calculated a series of electronic properties, consisting of partial electronic density of states (PDOS), the average Bader charge, the 3D charge-density difference, and the sliced electron localization function. As displayed in Fig. 7b and Fig. S20, the d-band centers of S-Mo₂C, S-MoP, are -1.63, -1.23, -1.93, and -1.87 eV, more remote from the Fermi level (E_F) than those in the corresponding Mo₂C (-1.60 eV), MoP (-0.96 eV), MoN (-1.80 eV), MoO₃ (-1.17 eV) respectively. This result suggests that the doping of S atoms in MoX_n can downshift the d-band center of Mo and facilitate the H desorption, which is beneficial for improving the electrocatalytic HER performance [43]. Furthermore, we calculated the average Bader charges (Table S3) of the optimized H* coordinated site on simulated models as H-MoS₂, H-Mo₂C, H-S-Mo₂C, H-MoP, H-S-MoP, H-S-MoN, and H-S-MoO₃. The average Bader charges of all metallic Mo atoms in MoX_n are negative, while that of non-metallic atoms (S, C, P, N, and O) are positive, demonstrating the charge transfer from metallic Mo to nonmetals. Moreover, the average Bader charges of Mo in H-S-Mo₂C (-0.662) and H-S-MoP (-0.562) are more negative than those in H-Mo₂C (-0.658) and H-MoP (-0.559), indicating that the extra charge

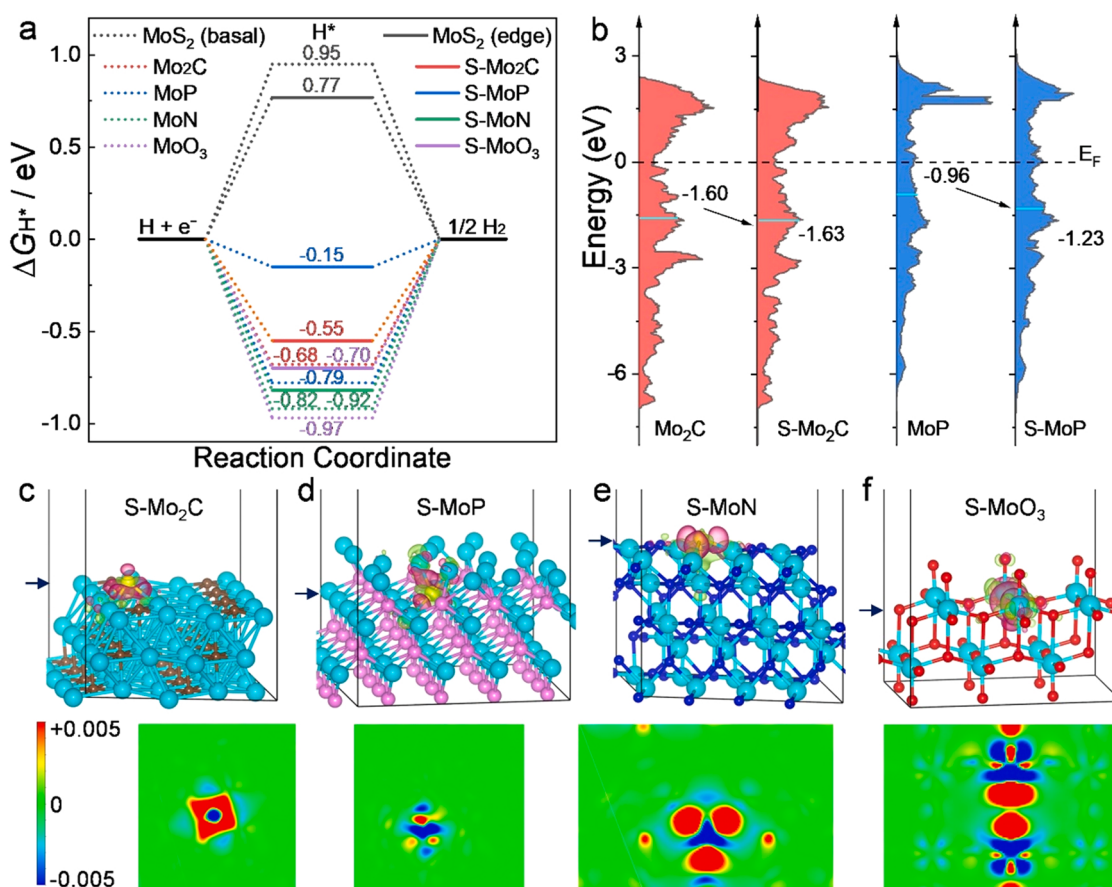


Fig. 7. (a) The free-energy diagram of the HER on various models; (b) The partial electronic density of states (PDOS) for d orbital of Mo₂C, S-Mo₂C, MoP, and S-MoP; the d-band centers of Mo atoms are labeled by cyan lines and black fonts; (c-f) The 3D charge density differences and the sliced electron localization function of S atom through the simulation models of S-Mo₂C, S-MoP, S-MoN, and S-MoO₃, respectively, in which the Mo, C, P, N, and O atoms are marked in cyan, gray, pink, blue, and red, respectively. The red and green shadows represent charge accumulation and depletion, with iso-surface = 0.005 e bohr⁻³.

transfer from Mo to C, P and S, which matches well with the XPS results. To some extent, the dopant S can adjust the electron distribution of adjacent atoms in the lattice and regulate the appropriate charge density of the catalysts. Notably, the 3D charge density differences and the sliced electron localization function of S (Fig. 7c-f) further reveal the positive effect of S dopant can reform the delocalized electron distribution of S-MoX_n to generate more active sites for boosting HER performance [31].

4. Conclusion

In summary, a universal *in situ* sulfur-doping strategy was developed to construct self-supported monolithic electrodes of sulfur-doped molybdenum-based compounds nanosheets on CC (S-Mo₂C/CC, S-MoP/CC, S-MoN/CC, and S-MoO₃/CC) via pyrolyzing MoS₂/CC precursor under different atmospheres. Various characterization and theoretical calculation results show the superior HER performance of S-MoX_n/CC to those of MoS₂/CC and MoX_n/CC may mainly be related to the formation of HER-favorable phases of MoP and Mo₂C, as well as the synergistic effect between the alien S atoms *in situ* embedded in the lattice of MoX_n, which can effectively tune the electronic structure of MoX_n and optimize the ΔG_{H^+} . Accordingly, the optimized S-MoP/CC electrode exhibits superior HER performance with η_{10} of only 75, 75, and 127 mV in acidic, alkaline, and neutral media, and which can maintain a 30 h HER stability at a large current density. This work not only paves a viable route to design and fabricate versatile, high-activity and stable molybdenum-based HER electrocatalysts in a pH-universal environment, but also helps to understand the synergistic enhancement effect of doped non-metals for promoting the electrocatalytic performance of molybdenum-based compounds.

CRediT authorship contribution statement

B.L. and **J.Z.** conceived the idea, designed the research, and guided experiments and data analysis; **M.H.** and **H.C.** carried out experiments with the technical support of **X.G.**, **X.W.** and **R.Y.**; **M.H.** and **R.G.** carried out the DFT calculations; **M. H.** wrote the original manuscript. **B.L.** revised the manuscript; **P.J.** and **X.X.** provided suggestions for analyzing the experiments in the manuscript. All authors contributed to interpreting the results and revising the manuscript.

Declaration of Competing Interest

The authors declare that they have no known competing financial interests or personal relationships that could have appeared to influence the work reported in this paper.

Data availability

The authors do not have permission to share data.

Acknowledgement

The financial support from the National Natural Science Foundation of China (NSFC) (21971129, 21961022, 22172083, and 21962013), Inner Mongolia Autonomous Region 2022 Leading Talent Team of Science and Technology (2022LJRC0008), the Natural Science Foundation of Inner Mongolia Autonomous Region of China (2022MS02014, 2021BS02007, and 2021JQ02), the 111 Project (D20033), the Program of Higher-level Talents of IMU (21300-5215101, 21300-5185111, and 21300-5195109), the “Grassland Leading Talent” Program of Inner Mongolia, the “Grassland Talent” Innovation Team of Inner Mongolia, the “Science and Technology for a Better Development of Inner Mongolia” Program (2020XM03), and the Science and Technology Project of Ordos (2021 ZDI 11-14).

Appendix A. Supporting information

Supplementary data associated with this article can be found in the online version at doi:10.1016/j.apcatb.2022.122131.

References

- S. van Renssen, The hydrogen solution? Nat. Clim. Change 10 (2020) 799–801, <https://doi.org/10.1038/s41558-020-0891-0>.
- J. Zhu, L. Hu, P. Zhao, L.Y.S. Lee, K.Y. Wong, Recent advances in electrocatalytic hydrogen evolution using nanoparticles, Chem. Rev. 120 (2020) 851–918, <https://doi.org/10.1021/acs.chemrev.9b00248>.
- K. Liang, S. Pakhira, Z. Yang, A. Nijamudheen, L. Ju, M. Wang, C.I. Aguirre-Velez, G.E. Sterbinsky, Y. Du, Z. Feng, J.L. Mendoza-Cortes, Y. Yang, S-doped MoP nanoporous layer toward high-efficiency hydrogen evolution in pH-universal electrolyte, ACS Catal. 9 (2018) 651–659, <https://doi.org/10.1021/acscatal.8b04291>.
- Z. Liu, K. Nie, X. Qu, X. Li, B. Li, Y. Yuan, S. Chong, P. Liu, Y. Li, Z. Yin, W. Huang, General bottom-up colloidal synthesis of nano-monolayer transition-metal dichalcogenides with high 1T'-phase purity, J. Am. Chem. Soc. 144 (2022) 4863–4873, <https://doi.org/10.1021/jacs.1c12379>.
- L. Wang, G. Qi, X. Liu, Sulfur dopant-enhanced neutral hydrogen evolution performance in MoO₃ nanosheets, Nanotechnology 33 (2022), 065701, <https://doi.org/10.1088/1361-6528/ac33d2>.
- X.F. Zhou, Y.H. Tian, J. Luo, B. Jin, Z.J. Wu, X.M. Ning, L. Zhan, X.L. Fan, T. Zhou, S.Q. Zhang, X.S. Zhou, Mo quantum Dots@N-doped-carbon for low-cost and efficient hydrogen evolution reaction: from electrocatalysis to photocatalysis, Adv. Funct. Mater. 32 (2022) 2201518, <https://doi.org/10.1002/adfm.202201518>.
- C. Pi, C. Huang, Y. Yang, H. Song, X. Zhang, Y. Zheng, B. Gao, J. Fu, P.K. Chu, K. Huo, In situ formation of N-doped carbon-coated porous MoP nanowires: a highly efficient electrocatalyst for hydrogen evolution reaction in a wide pH range, Appl. Catal. B 263 (2020), 118358, <https://doi.org/10.1016/j.apcatb.2019.118358>.
- N. Yao, R. Meng, J. Su, Z. Fan, P. Zhao, W. Luo, Dual-phase engineering of MoN/Co₄N with tailored electronic structure for enhanced hydrogen evolution, Chem. Eng. J. 421 (2021), 127757, <https://doi.org/10.1016/j.cej.2020.127757>.
- Y. Xu, R. Wang, Z. Liu, L. Gao, T. Jiao, Z. Liu, Ni₂P/MoS₂ interfacial structures loading on N-doped carbon matrix for highly efficient hydrogen evolution, Green Energy Environ. 7 (2022) 829–839, <https://doi.org/10.1016/j.gee.2020.12.008>.
- Y. Xu, R. Wang, J. Wang, Z. Li, T. Jiao, Z. Liu, Facile fabrication of molybdenum compounds (Mo₂C, MoP and MoS₂) nanoclusters supported on N-doped reduced graphene oxide for highly efficient hydrogen evolution reaction over broad pH range, Chem. Eng. J. 417 (2021), <https://doi.org/10.1016/j.cej.2021.129233>.
- Y. Xu, R. Wang, J. Wang, Y. Zhang, T. Jiao, Encapsulation of Fe-CoP with P, N-codoped porous carbon matrix as a multifunctional catalyst for wide electrochemical applications, J. Energy Chem. 71 (2022) 36–44, <https://doi.org/10.1016/j.jec.2022.03.043>.
- K. Li, T. Jiao, R. Xing, G. Zou, J. Zhou, L. Zhang, Q. Peng, Fabrication of tunable hierarchical MXene@AuNPs nanocomposites constructed by self-reduction reactions with enhanced catalytic performances, Sci. China Mater. 61 (2018) 728–736, <https://doi.org/10.1007/s40843-017-9196-8>.
- H. Deng, J. Yin, J. Ma, J. Zhou, L. Zhang, L. Gao, T. Jiao, Exploring the enhanced catalytic performance on nitro dyes via a novel template of flake-network Ni-Ti LDH/GO in-situ deposited with Ag₃PO₄ NPs, Appl. Surf. Sci. 543 (2021), <https://doi.org/10.1016/j.apsusc.2020.148821>.
- Y. Tang, C. Yang, X. Yu, X. Kang, J. Henzie, W. Que, Y. Yamauchi, MXene nanoarchitectonics defect-engineered 2D MXenes towards enhanced electrochemical water splitting, Adv. Energy Mater. 12 (2022) 2103867, <https://doi.org/10.1002/aenm.202103867>.
- X. Zhang, X. Yu, L. Zhang, F. Zhou, Y. Liang, R. Wang, Molybdenum phosphide/carbon nanotube hybrids as pH-universal electrocatalysts for hydrogen evolution reaction, Adv. Funct. Mater. 28 (2018) 1706523, <https://doi.org/10.1002/adfm.201706523>.
- H. Li, M. Hu, L. Zhang, L. Huo, P. Jing, B. Liu, R. Gao, J. Zhang, B. Liu, Hybridization of bimetallic molybdenum-tungsten carbide with nitrogen-doped carbon: a rational design of super active porous composite nanowires with tailored electronic structure for boosting hydrogen evolution catalysis, Adv. Funct. Mater. 30 (2020) 2003198, <https://doi.org/10.1002/adfm.202003198>.
- Y. Yang, M. Luo, Y. Xing, S. Wang, W. Zhang, F. Lv, Y. Li, Y. Zhang, W. Wang, S. Guo, A universal strategy for intimately coupled carbon nanosheets/MoM nanocrystals (M = P, S, C, and O) hierarchical hollow nanospheres for hydrogen evolution catalysis and sodium-ion storage, Adv. Mater. 30 (2018) 1706085, <https://doi.org/10.1002/adma.201706085>.
- H. Li, M. Hu, B. Cao, P. Jing, B. Liu, R. Gao, J. Zhang, X. Shi, Y. Du, Multi-elemental electronic coupling for enhanced hydrogen generation, Small 17 (2021) 2006617, <https://doi.org/10.1002/smll.202006617>.
- M. Ding, H. Xu, M. Liu, Y. Wang, A. Wang, T. Lin, L. Zhang, K. Zhang, Interface construction and porosity engineering to trigger efficient hydrogen evolution of two-dimensional porous molybdenum phosphide/dioxide heterojunction nanosheets in acidic and alkaline electrolytes, Chem. Eng. J. 430 (2022), 132674, <https://doi.org/10.1016/j.cej.2021.132674>.
- Z. Zhao, F. Qin, S. Kasiraju, L. Xie, M.K. Alam, S. Chen, D. Wang, Z. Ren, Z. Wang, L.C. Grabow, J. Bao, Vertically aligned MoS₂/Mo₂C hybrid nanosheets grown on

carbon paper for efficient electrocatalytic hydrogen evolution, *ACS Catal.* 7 (2017) 7312–7318, <https://doi.org/10.1021/acscatal.7b02885>.

[21] A. Wu, Y. Gu, Y. Xie, C. Tian, H. Yan, D. Wang, X. Zhang, Z. Cai, H. Fu, Effective electrocatalytic hydrogen evolution in neutral medium based on 2D MoP/MoS₂ heterostructure nanosheets, *ACS Appl. Mater. Interfaces* 11 (2019) 25986–25995, <https://doi.org/10.1021/acsmi.9b07415>.

[22] Y. Cheng, J. Gong, B. Cao, X. Xu, P. Jing, S.-P. Feng, R. Cheng, B. Liu, R. Gao, J. Zhang, Ultrafine VN nanodots induced generation of abundant cobalt single-atom active sites on nitrogen-doped carbon nanotube for efficient hydrogen evolution, *J. Energy Chem.* 68 (2022) 646–657, <https://doi.org/10.1016/j.jecchem.2021.11.035>.

[23] B. Cao, Y. Cheng, M. Hu, P. Jing, Z. Ma, B. Liu, R. Gao, J. Zhang, Efficient and durable 3D self-supported nitrogen-doped carbon-coupled nickel/cobalt phosphide electrodes: stoichiometric ratio regulated phase- and morphology-dependent overall water splitting performance, *Adv. Funct. Mater.* 29 (2019) 1906316, <https://doi.org/10.1002/adfm.201906316>.

[24] M. Hu, H. Chen, B. Liu, X. Xu, B. Cao, P. Jing, J. Zhang, R. Gao, J. Zhang, Coupling ceria with dual-phased molybdenum carbides for efficient and stable hydrogen evolution electrocatalysis at large-current-density in freshwater and seawater, *Appl. Catal. B* 317 (2022), <https://doi.org/10.1016/j.apcatb.2022.121774>.

[25] C. Tang, W. Wang, A. Sun, C. Qi, D. Zhang, Z. Wu, D. Wang, Sulfur-decorated molybdenum carbide catalysts for enhanced hydrogen evolution, *ACS Catal.* 5 (2015) 6956–6963, <https://doi.org/10.1021/acscatal.5b01803>.

[26] R. Ye, P. del Angel-Vicente, Y. Liu, M.J. Arellano-Jimenez, Z. Peng, T. Wang, Y. Li, B.I. Yakobson, S.H. Wei, M.J. Yacaman, J.M. Tour, High-performance hydrogen evolution from MoS_{2(1-x)}P_(x) solid solution, *Adv. Mater.* 28 (2016) 1427–1432, <https://doi.org/10.1002/adma.201504866>.

[27] J. Xie, H. Zhang, S. Li, R. Wang, X. Sun, M. Zhou, J. Zhou, X.W. Lou, Y. Xie, Defect-rich MoS₂ ultrathin nanosheets with additional active edge sites for enhanced electrocatalytic hydrogen evolution, *Adv. Mater.* 25 (2013) 5807–5813, <https://doi.org/10.1002/adma.201302685>.

[28] G. Kresse, J. Furthmüller, Efficient iterative schemes for ab initio total-energy calculations using a plane-wave basis set, *Phys. Rev. B Condens. Matter Mater. Phys.* 54 (1996) 11169–11186, <https://doi.org/10.1103/physrevb.54.11169>.

[29] G. Kresse, D. Joubert, From ultrasoft pseudopotentials to the projector augmented-wave method, *Phys. Rev. B Condens. Matter Mater. Phys.* 59 (1999) 1758–1775, <https://doi.org/10.1103/PhysRevB.59.1758>.

[30] J.P. Perdew, K. Burke, M. Ernzerhof, Generalized gradient approximation made simple, *Phys. Rev. Lett.* 77 (1996) 3865–3868, <https://doi.org/10.1103/PhysRevLett.77.3865>.

[31] X. Huang, H. Xu, D. Cao, D. Cheng, Interface construction of P-substituted MoS₂ as efficient and robust electrocatalyst for alkaline hydrogen evolution reaction, *Nano Energy* 78 (2020), 105253, <https://doi.org/10.1016/j.nanoen.2020.105253>.

[32] Q. Wang, X. Li, X. Ma, Z. Li, Y. Yang, Activation of the MoS₂ basal plane to enhance CO hydrogenation to methane activity through increasing S vacancies, *ACS Appl. Mater. Interfaces* 14 (2022) 7741–7755, <https://doi.org/10.1021/acsmi.1c18291>.

[33] C. Wu, M.A. Nahil, N. Miskolci, J. Huang, P.T. Williams, Processing real-world waste plastics by pyrolysis-reforming for hydrogen and high-value carbon nanotubes, *Environ. Sci. Technol.* 48 (2014) 819–826, <https://doi.org/10.1021/es402488b>.

[34] L. Chen, M. Zeng, W. Zhang, L. He, W. He, F. Yang, X. Zhang, Morphology-controlled synthesis of molybdenum disulfide wrapped single-walled carbon nanotubes for the hydrogen evolution reaction, *ChemCatChem* 10 (2018) 1128–1133, <https://doi.org/10.1002/cctc.201701403>.

[35] Y.-Y. Ma, C.-X. Wu, X.-J. Feng, H.-Q. Tan, L.-K. Yan, Y. Liu, Z.-H. Kang, E.-B. Wang, Y.-G. Li, Highly efficient hydrogen evolution from seawater by a low-cost and stable CoMoP@C electrocatalyst superior to Pt/C, *Energy Environ. Sci.* 10 (2017) 788–798, <https://doi.org/10.1039/c6ee03768b>.

[36] M. He, H. Shi, X. Sun, B. Gao, Porous Mo₂C–MoP heterostructure on carbon cloth for efficient hydrogen evolution reaction over a broad pH range, *ChemCatChem* 13 (2020) 966–974, <https://doi.org/10.1002/cctc.202001639>.

[37] S. Adamiak, W. Bochnowski, A. Dziedzic, L. Szylner, D. Adamiak, Characteristics of the structure, mechanical, and tribological properties of a Mo–Mo₂N nanocomposite coating deposited on the Ti₆Al₄V alloy by magnetron sputtering, *Materials* 14 (2021) 6819, <https://doi.org/10.3390/ma14226819>.

[38] G.U.M., D. VariSli, Multiwall carbon nanotube-supported molybdenum catalysts for ammonia decomposition reaction under microwave effect, *Turk. J. Chem.* 44 (2020) 309–324, <https://doi.org/10.3906/kim-1907-4>.

[39] A.K. Datye, Q. Xu, K.C. Kharas, J.M. McCarty, Particle size distributions in heterogeneous catalysts: what do they tell us about the sintering mechanism, *Catal. Today* 111 (2006) 59–67, <https://doi.org/10.1016/j.cattod.2005.10.013>.

[40] H. Chen, M. Hu, P. Jing, B. Liu, R. Gao, J. Zhang, Constructing heterostructure of CeO₂/WS₂ to enhance catalytic activity and stability toward hydrogen generation, *J. Power Sources* 521 (2022), 230948, <https://doi.org/10.1016/j.jpowsour.2021.230948>.

[41] G. Zhao, K. Rui, S.X. Dou, W. Sun, Heterostructures for electrochemical hydrogen evolution reaction: a review, *Adv. Funct. Mater.* 28 (2018) 1803291, <https://doi.org/10.1002/adfm.201803291>.

[42] Y.J. Kim, A. Lim, J.M. Kim, D. Lim, K.H. Chae, E.N. Cho, H.J. Han, K.U. Jeon, M. Kim, G.H. Lee, G.R. Lee, H.S. Ahn, H.S. Park, H. Kim, J.Y. Kim, Y.S. Jung, Highly efficient oxygen evolution reaction via facile bubble transport realized by three-dimensionally stack-printed catalysts, *Nat. Commun.* 11 (2020) 4921, <https://doi.org/10.1038/s41467-020-18686-0>.

[43] R. Gao, L. Pan, H. Wang, X. Zhang, L. Wang, J.-J. Zou, Ultradispersed nickel phosphide on phosphorus-doped carbon with tailored d-band center for efficient and chemoselective hydrogenation of nitroarenes, *ACS Catal.* 8 (2018) 8420–8429, <https://doi.org/10.1021/acscatal.8b02091>.